Composites Part C: Open Access 20 (2026) 100775

Contents lists available at ScienceDirect

Composites Part C: Open Access

journal homepage: www.elsevier.com/locate/composites-part-c-open-access

Screen-printed polyetherimide smart inlays for surveillance of bonded joints in composite structures

Ann-Kathrin Klein [a,*], Riem Kilian [b], Chresten von der Heide [a], Julian Steinmetz [b], Christian Hühne [b,c], Oliver Völkerink [b], Andreas Dietzel [a]

[a] Institute of Microtechnology, Technische Universität Braunschweig, Alte Salzdahlumer Str. 203, Braunschweig, 38124, Germany
[b] Institute of Mechanics and Adaptronics, Technische Universität Braunschweig, Langer Kamp 6, Braunschweig, 38106, Germany
[c] Institute of Lightweight Systems, German Aerospace Center (DLR), Lilienthalplatz 7, Braunschweig, 38108, Germany

ARTICLE INFO

Dataset link: https://doi.org/10.5281/zenodo.15479526

Keywords:
Screen-printing
Carbon ink
Adhesive bondline
Composite
Structural health monitoring

ABSTRACT

Adhesive bonding is ideal for joining lightweight components made of composite materials. However, the reliability of these structural bonds, particularly in terms of fatigue crack growth, is a major concern. To mitigate this risk, structural health monitoring of the bonding is desired. This can be achieved by measuring strains at different locations in the adhesive bondline. Here, we present screen-printing on polyetherimide to realize a smart inlay that can be placed into the adhesive bondline during CFRP integration and can replace cleanroom-fabricated crack propagation sensors demonstrated earlier. The sensor layout is designed to enable crack monitoring by evaluating strain differences between two sensor rows. For the first time, smart inlays were fabricated and encapsulated entirely on polyetherimide, which has excellent adhesion strength to the epoxy matrix of CFRP. For strain detection, we used screen-printed carbon sensors. We selected screen-printing inks that could withstand the harsh conditions during CFRP fabrication. For the characterization of our smart inlay, we analyzed the screen-printed carbon sensors before and after integration into composites. After integration, the sensors were fully functional. As a striking result, after the entire fabrication and integration, the sensitivity of the screen-printed carbon sensors reached a gauge factor of up to 49.

1. Introduction

Reducing the overall weight is an important approach to lowering the energy consumption in all moving vehicles, particularly in the aviation industry. For this reason, the use of carbon fiber-reinforced polymer (CFRP) and its adhesive bonding is becoming more and more important. CFRP can meet mechanical requirements due to its high strength, high stiffness, and durability. Adhesive bonding is ideal for joining lightweight components made of composite materials as it is mechanically superior to bolted joints. However, the reliability of this structural bonding is an important concern, and failure due to fatigue is a stochastic phenomenon and difficult to predict. To reduce this risk, approaches often accept lower material efficiency, resulting in higher weight. Structural health monitoring can be the solution to exploit the full composite lightweight potential. For adhesively bonded CFRP structures, the detection of crack initiation and crack propagation in the bondline is particularly important, as these damage mechanisms affect the structural integrity under operational loads. The relevant state of the art on crack detection not only includes the perspective of sensing capability, but also aspects of material compatibility, integration into the structure, manufacturing effort, and possible effects on adhesive performance, such as bond strength.

Since the internal strains are relevant, externally applied commercially available strain sensors are unsuitable, and may not even have sufficient fatigue resistance for long-term monitoring [1]. Although ex-situ methods such as ultrasonic techniques, X-ray, and thermography are still used, they are usually labor-intensive and sometimes only applicable after disassembly [2]. Therefore, several research groups are working on strain measurement in the adhesive bondline between two composite adherends. So far, mainly fiber optical sensors [1,3–6] were used. They have the disadvantage that they usually require additional optoelectronic components and complex mathematical evaluation features. More recently, functionalized adhesive films by adding nanoparticles like carbon nanotubes (CNTs) were studied [7–10]. These films can directly detect strain through changes in electrical signal. However, adding the CNT can reduce the failure strain [11]. Another method is to use so-called z-pins combined with resistance measurement [12]. The z-pins are short metal rods arranged in the z-direction of a lap joint acting as a crack-arrest mechanism [12]. The additional eddy

* Corresponding author.
E-mail address: ann-kathrin.klein@tu-braunschweig.de (A.-K. Klein).

https://doi.org/10.1016/j.jcomc.2026.100775
Received 2 March 2026; Received in revised form 10 June 2026; Accepted 7 July 2026
Available online 14 July 2026

current (EC) sensing film can detect a potential crack [13,14]. However, it is quite time-consuming to embed the z-pins and EC sensing films. In addition, the data evaluation is complex, and it has not yet been investigated whether the mechanical performance is restricted [2]. So, crack detection concepts differ not only in sensing principle, but also in their material systems, processing routes, integration effort, and cost [15]. Methods for measuring crack initiation and propagation should provide direct in-situ information from the bondline, require only moderate instrumentation and data processing, be compatible with scalable and cost-efficient manufacturing, and have little or no adverse effect on the adhesive joint. Existing approaches only partially meet these requirements. Fiber-optic systems are sensitive but relatively complex and costly in terms of instrumentation [16]. Functionalized adhesive layers offer direct electrical sensing, but the conductive fillers may alter the mechanical properties of the adhesive [17]. Z-pins combine reinforcement and monitoring, but require complex integration steps and may affect structural performance [18]. EC sensing does not detect cracks that do not cross or interfere with the current and thus may compromise the integrity of the component [19]. These limitations show that the integration strategy itself strongly influences both sensing reliability and adhesive joint behavior.

Our group has researched smart inlays based on strain gauges that can be placed into the adhesive bondline during CFRP integration to detect and measure potential crack propagation during operational load. Combined with a surface toughening method, this inlay should stop a potential crack. In addition, this inlay should not weaken the adhesive bondline. In our previous work, we developed smart inlays where micro-strain sensor structures were directly applied on crack-resistant polyvinylidene fluoride (PVDF) films, so-called disbond arrest features (DAF) [20]. However, without mechanical reinforcement, the thin metallic microstructures could float in the surrounding melt during CFRP integration in composites and thus be deformed and destroyed after cooling. Recently, polyetherimide (PEI), which has a significantly higher melting point, was used as a carrier film for microsensors instead of PVDF [21]. Subsequently, PVDF was used multifunctionally, on the one hand to encapsulate the sensors and on the other hand as DAF. In this way, the crack detection capability of the approach was demonstrated. In cyclic crack growing tests, crack detection within the first 50,000 cycles and detection when the crack reaches the DAF could be shown [21]. However, the interfaces between PEI and PVDF of the integrated smart inlay often led to the failures of the fabricated composites [22,23]. Moreover, the entire microfabrication and integration process was unsuitable for production scale-up.

In this work, we aim to achieve progress in the smart inlay integration and robustness to improve crack detection. By completely encapsulating the smart inlay with PEI, which is known for its excellent adhesion strength to the epoxy matrix of CFRP due to diffusion during the curing process [24–27] and less influence on the tensile strength [28], the integration of the smart inlay should be improved, and the precision of crack detection should be increased. Moreover, using cost-efficient screen-printing of the strain sensors opens up the opportunity for a more streamlined production process. In addition, screen printing not only speeds up production compared to lithographic fabrication but can also be easily scaled for larger production quantities. The use of stretchable and highly sensitive inks in screen printing further improves the prospects for applications under dynamic load conditions. Research into the electromechanical properties of screen-printing inks and requirements placed on the materials by sensor integration in harsh environments could provide valuable insights for future developments in this area. Thus, the present work focuses on improved smart inlay integration and robustness. A dedicated mechanical assessment of bonded joints containing the smart inlay was not part of the present study; the corresponding bonded-joint behavior has been investigated separately using bonded DCB and ENF specimens and will be reported elsewhere.

2. Experimental

2.1. Smart inlay design

The smart inlay design consisted of four sensor bridges, each arranged in pairs in two rows. DAFs were placed in the area of the sensor rows to stop a potential crack. The smart inlay and the DAFs were integrated into the CFRP component so that a potential crack front through the adhesive bondline first reached the first row of sensors. The sensor rows had a distance of 10 mm and were each 10 mm wide; the functionality for these dimensions has already been shown previously [29]. Each sensor row in the screen-printed smart inlay consisted of two Wheatstone bridges (Fig. 1).

2.2. Material selection

PEI with a thickness of 125 µm was used as the substrate material for the sensors to ensure sufficient stability during handling in the screen-printing process. For encapsulation of the smart inlay, PEI with a thickness of 25 µm was utilized. The compatibility of PEI for integration into CFRP in terms of processing compatibility, thermal stability, and adhesion to epoxy has already been demonstrated in earlier works [24,28]. It showed a high interfacial adhesion on epoxy-based CFRP without affecting the strength of CFRP.

The primary selection criterion for the screen-printing inks was the sensor functionality after annealing due to integration with the prepreg-autoclave process. The selection was made from three available commercial inks (Saral StretchCarbon 100, DuPont PE 671 and Dycotec DM-CAP-2101). Saral StretchCarbon 100 was selected because of its reliable performance after integration. An ink with low resistance was selected for the conductor tracks, and one with relatively high resistance for the sensors, to reduce the influence of longer conductor tracks on the sensor signal, even in sensor networks with long tracks.

2.3. Smart inlay film fabrication and integration

For the smart inlay, a 125 µm thin PEI film (ULTEM 1000B, Vink König Deutschland GmbH, Wuppertal, Germany) was used as substrate material. Screen-printing was used to functionalize the film with strain sensors. As the surfaces of PEI film have different surface quality, the next steps were carried out on either the smooth or the rough surface to evaluate the more suitable surface quality for screen-printing. All printing steps were done under ambient conditions with a semiautomatic flat screen-printing machine Sirimac 6080 E. Screen printing was carried out at a printing speed of 106 $mm \cdot s^{-1}$ using a machine pressure setting of 2.5 bar, a squeegee angle of 45°, and 15 printing passes. A high-strength stainless-steel mesh (KOENEN GmbH, Ottobrunn-Riemerling, Germany) with different patterns with a mesh size of 53 µm and a wire thickness of 24 µm was used for the screen printing. To prevent the substrate films from shrinking during the curing steps, the substrate films were pre-treated in an oven at 130 °C for 90 min. First, the conductive paths were printed in the desired pattern using silver ink (DM-SIP-2006, Dycotec, Calne, United Kingdom) (Fig. 2a). The printed silver layer was cured at 120 °C for 5 min in an oven. Then, a carbon layer was printed for the high-resistance resistors using carbon ink (Saral StretchCarbon 100, Saralon GmbH, Chemnitz, Germany) (Fig. 2b). The ink was dried at 120 °C for 5 min in an oven. The thickness of silver and carbon ink on PEI was examined in this paper. The sensor structures were encapsulated with a second 25 µm thin PEI Ultem 1000 film using diffusion bonding at 230 °C in a preheated oven for 60 min under vacuum (Fig. 2c). Subsequently, the smart inlays were integrated into the composite components during co-curing in the prepreg-autoclave process. The applied curing cycle was described in earlier work [20]. After integration, samples with a cross-section of 25 mm × 200 mm were separated by saw cutting.

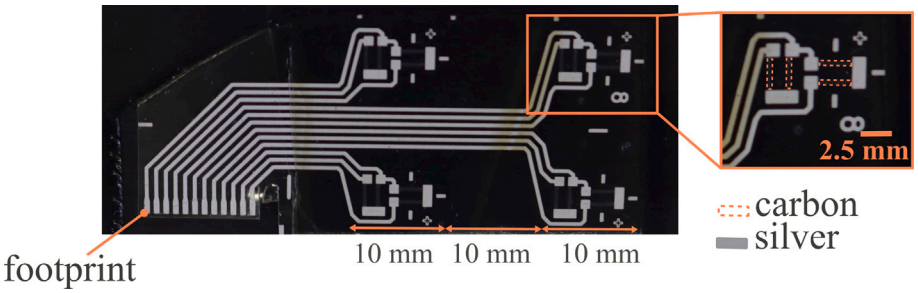

Fig. 1. Photograph illustration concept and design of screen-printed smart inlays integrated on CFRP. The zoom on the right shows our Wheatstone sensor bridge with a longitudinal and a transversal sensor. The variable longitudinal sensor, in particular, has an influence on the change in our sensor signal.

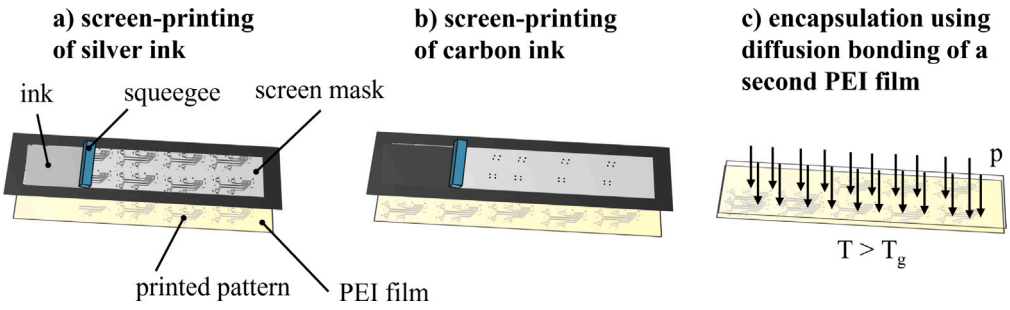

Fig. 2. Schematic illustration of smart inlay fabrication: (a) screen-printing of silver layer on pretreated PEI film. (b) screen-printing of carbon layer on cured silver layer. (c) encapsulation of functionalized PEI film with second PEI film on top using diffusion bonding.

2.4. Sensor characterization

The topography of the screen-printed layers was measured by LSM (confocal laser scanning microscope VK-X260, Keyence, Osaka, Japan). Roughness was measured at 150x magnification according to DIN 25178. Optical evaluations of the morphology and manufacturability of the screen-printed layers were analyzed using an optical microscope (VHX-5000, Keyence, Osaka, Japan) and SEM (scanning electron microscope Phenom XL, Thermo Fisher Scientific Inc., Waltham, MA, USA). Resistance and current–voltage characteristics were measured between silver ink electrodes using a source meter (Keithley 2450, Tektronix, Inc., Beaverton, OR, USA) in two-point mode. Here, the measured values were in the kΩ-range, so the influence of the contact and line resistances in a two-point configuration was negligible [17]. Silver ink electrodes have practically no influence on the carbon sensor resistance, even after encapsulation and integration. All measurements were performed under ambient conditions. Sheet resistance R_s was calculated as $R_s = R \cdot w/l$ with screen-printed line width w, and line length l. For piezoresistive characterization of sensor paths were loaded to a maximum strain of 2305 µm·m^{-1} with a strain rate of 2.46 mm·s^{-1}. For this purpose, a custom-designed tensile testing machine was used in which the specimens can be clamped, electrically connected with spring-loaded pins, and stretched using a stepper motor; the step size, maximum strain, and stretch speed could be adjusted. The gauge factor GF representing the piezoresistive sensitivity is defined as $GF = \frac{\Delta R/R_0}{\varepsilon}$, where ΔR is the change of resistance, R_0 the initial resistance, and $\varepsilon = \Delta l/l_0$ the longitudinal strain calculated based on crosshead displacement Δl, evaluated using a position sensor.

2.5. Tensile tests of PEI film, smart inlays, and integrated smart inlays in composite

The mechanical tests were carried out in a three-stage sequence of static tensile testing as illustrated in (cf. Fig. 3). In the first stage, pure PEI film and fusion-bonded PEI film were tested. PEI film was cut into specimens (ASTM D638 Type V specimen) using a femtosecond laser. The measuring length was 25.4 mm. The tensile testing machine with a load cell up to 5 kN (zwickiLine Z.5.0, ZwickRoell GmbH & Co. KG, Ulm, Germany) was used for these tests. The PEI film samples were first preloaded to 1 N and then the samples were stretched at a rate of 0.033 mm s^{-1} until they failed mechanically. The tensi,le test was performed and the results were evaluated according to the ASTM D638 standard. A total of four to five samples of each specimen were used for evaluation. Young's modulus was calculated by applying Hooke's law to the measured stress–strain curve.

In the second stage, the non-integrated, pure smart inlay film was stretched in a tensile testing machine until the sensors failed electrically. The tensile testing machine with a load cell up to 1 kN (zwickiLine Z1.0, ZwickRoell GmbH & Co. KG, Ulm, Germany) was used for these tests. For this purpose, the smart inlay films were cut out slightly larger so they could be clamped into the test machine at the top and bottom. In this way, the measuring length was 75 mm. The footprint of the smart inlay was electrically connected to a ZIF connector. A multi-channel strain gauge amplifier (QuantumX MX1616B, HBM, Darmstadt, Germany) was used for piezoresistive sensor signal evaluation. The bridge output was recorded at a sampling rate of 200 Hz and low-pass filtered using a 20 Hz Bessel filter. The smart inlay films were first preloaded to 2 N, and the sensor signal was set to zero. Then, the smart inlay films were stretched at a rate of 0.8 mm s^{-1} until they electrically failed.

In the third stage, the encapsulated smart inlay integrated into the composite was loaded in tension and unloaded ten times. The CFRP samples had a cross-section of 25 × 200 mm and a measuring length of 160 mm. As in the previous test, the footprint of the smart inlay was electrically connected to a ZIF connector. For piezoresistive sensor signal evaluation, the multi-channel strain gauge amplifier from the second stage was used. The force-controlled tensile testing machine with a load cell up to 25 kN (Amsler HC 25, ZwickRoell GmbH & Co. KG, Ulm, Germany) was used for these tests. The sample was first loaded once up to a maximum force of 3.033 kN (corresponding to an elongation of 1,196 µm·m^{-1}) within 10 s, the force was held for 20 s and then unloaded up to 0 N in 10 s. The sensor signal was set to zero after this cycle, and the same cycle was then carried out automatically ten times.

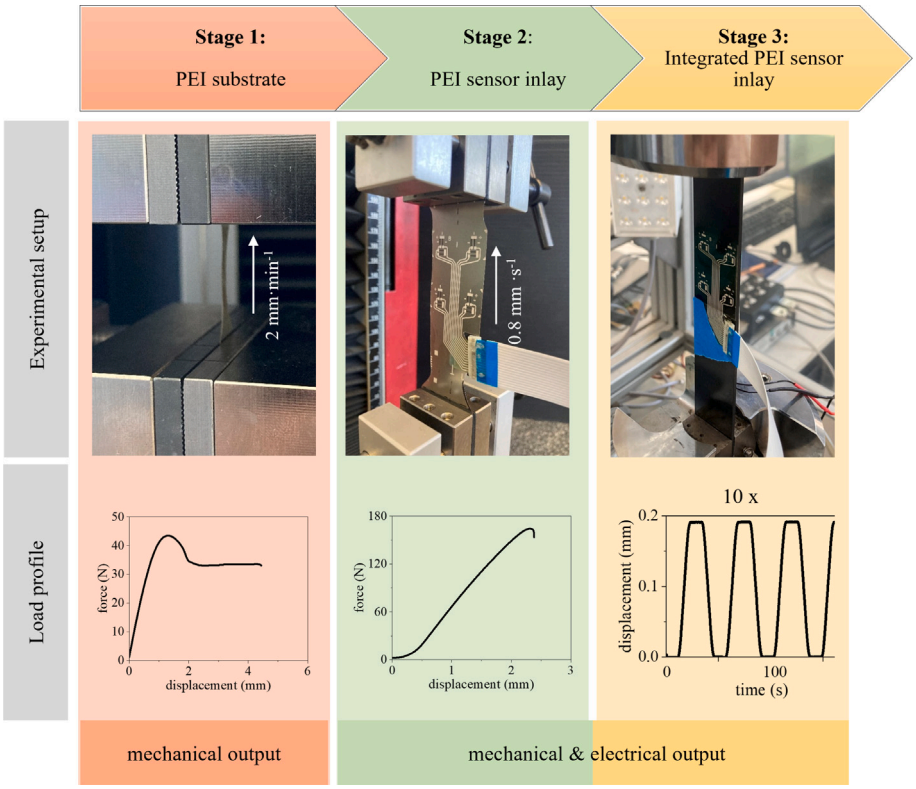

Fig. 3. Three-stage tensile testing sequence: In stage 1, PEI film substrate was tensile tested with preload of 1 N and then with a strain rate of 2 mm·s^{-1}. In stage 2, the PEI smart inlay was tensile tested with a preload of 2 N and then with a strain rate of 0.8 mm·s^{-1}. In stage 3, the integrated PEI smart inlay in the composite was loaded in tension and unloaded ten times. The output was mechanically for stage 1 and mechanically & electrically for stage 2 & 3.

The results of the second and third stages were also used to investigate sensor properties such as sensitivity, linearity, and hysteresis. The sensor signal was defined as $S = V_D/V_S$, where V_D is the signal of the Wheatstone bridge and V_S is the supply voltage. Two sensor paths are arranged orthogonally to one another. When subjected to a tensile test, one path is stretched longitudinally, whilst the other is stretched transversely. The latter therefore contracts as a result of the Poisson effect. The sensor signal thus incorporates the longitudinal strain ε of one path and the transverse strain $\varepsilon \cdot (1 + \nu)$ of the orthogonal sensor, where ν is the Poisson ratio (0.36 for all setups taken from data sheet for ULTEM 1000B and derived for the CFRP layup [21]). For the implemented Wheatstone half-bridge circuit with two orthogonal strain gauges, V_D can be expressed as $V_D = \frac{1}{4} \cdot GF \cdot V_S \cdot \varepsilon \cdot (1+\nu)$ [25] and GF was calculated as $GF = \frac{4 \cdot S}{\varepsilon \cdot (1+\nu)}$. The longitudinal strain $\varepsilon = \Delta l / l_0$ was calculated based on crosshead displacement Δl. Thus, the strain values used for the gauge factor calculation represent engineering strain estimates based on machine displacement rather than direct local strain measurements at the sensor position. This approach may involve uncertainty due to machine compliance, grip effects, and possible non-uniform strain fields within the specimen. For the integrated smart inlays, additional local strain measurements showed a 12 % lower local strain, indicating that the reported gauge factors for these samples are slightly underestimated and should be interpreted as effective values under the applied test conditions. For the other specimens, the error is estimated to be smaller, since the test specimens are orders of magnitude less rigid than the machine. Since all samples were evaluated using the same setup and procedure, the comparative assessment of the sensor response remains valid.

3. Results and discussion

3.1. Screen-printing of sensor structures

The commercial PEI film used had a smooth and a rough surface. This is due to the production process, as one surface comes into contact with the cooling roller after the extrusion, while the other side is exposed to a lower cooling rate [30]. We measured the line roughness of both PEI surfaces and investigated its influence on the fabrication of screen-printed sensors. The roughness characterization of the smooth and rough surfaces of the PEI film is shown in (Fig. 4a and 4b). The measured averaged roughness R_a is 0.406 ± 0.080 µm for the rough surface and 0.047 ± 0.012 µm for the smooth surface, which is less rough by one order of magnitude.

The roughness characterization of the printed and cured silver and carbon inks on smooth and rough PEI film surfaces is shown in Fig. 4c and 4d. The R_a of silver ink was 0.93 µm and 0.91 µm on rough and smooth surfaces, respectively. The R_a of carbon ink was 2.4 µm and 2.2 µm on rough and smooth surfaces, respectively. Considering the significant difference in surface quality between the two PEI film sides, substrate roughness did not appear to have a significant effect to the ink film roughness during screen-printing. The morphology of silver and carbon inks on rough surfaces is shown in SEM micrographs at various magnifications (Fig. 5). The cured inks formed an irregular, grainy, and opaque layer. In the case of silver ink, the layer consisted of monodisperse silver grains of the same type (0.5–5 µm). The carbon ink was polydisperse. The layer consisted of larger flakes (6.5–16 µm) and smaller grains (0.2–5 µm) analyzed from the SEM images. Smaller particles could not be found at the chosen magnification.

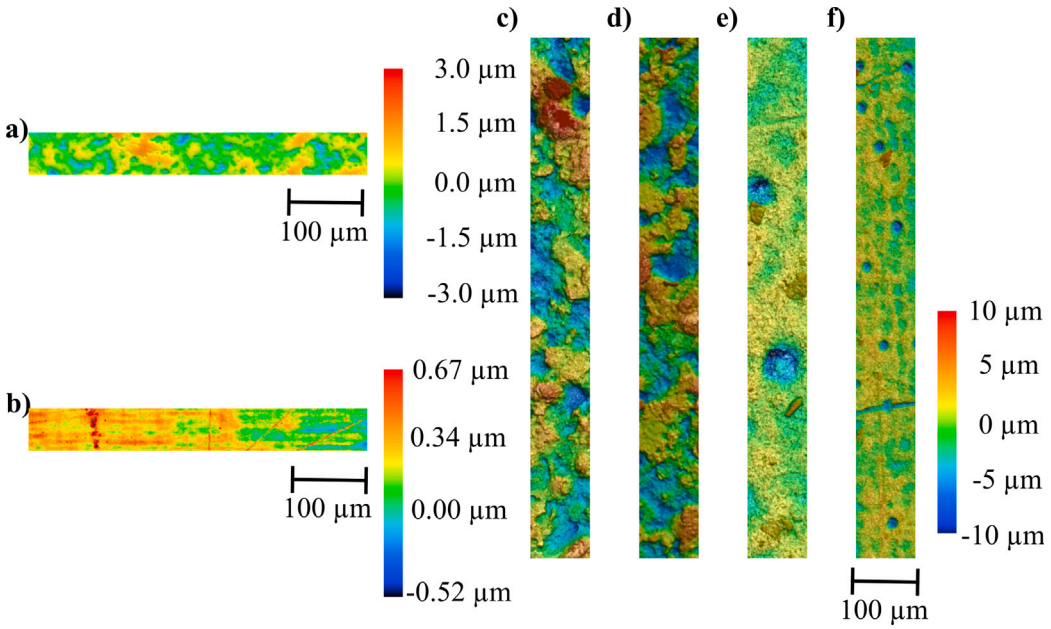

Fig. 4. Representative color-coded topographies generated by LSM of (a) rough PEI film surface. (b) smooth PEI film surface. (c-d) carbon ink on smooth and rough PEI film surface. (e-f) silver ink on smooth and rough PEI film surface.

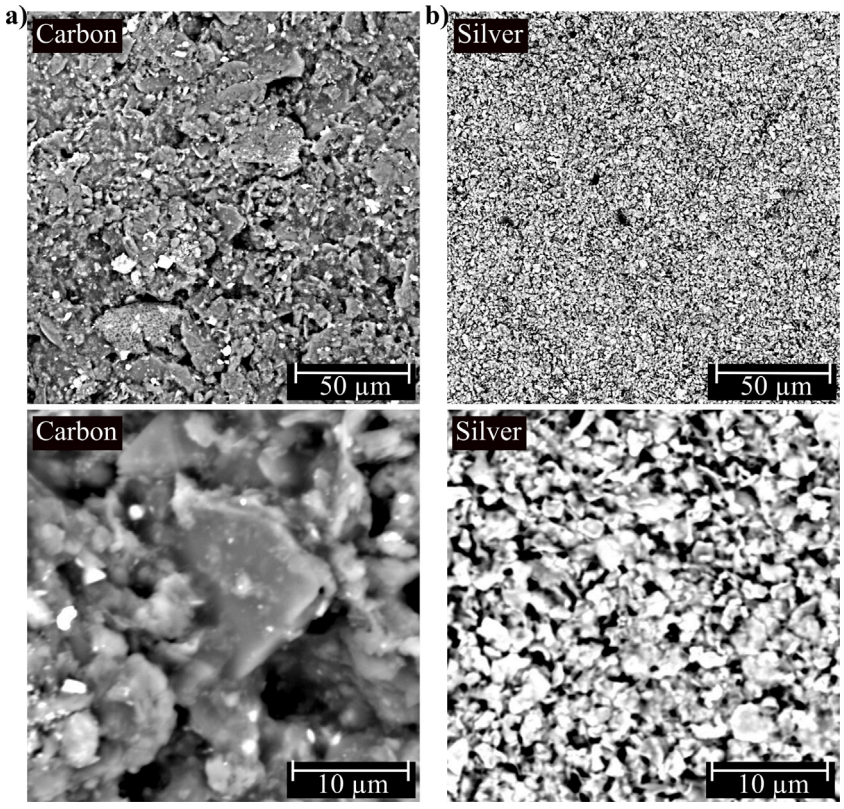

Fig. 5. Scanning electron images showing the morphology of (a) carbon ink at 860x (top) and 4400x (bottom) magnifications and, (b) silver ink at 860x (top) and 4400x (bottom) magnifications.

In addition to the roughness and morphology of the screen-printed inks, the real line width w and line height h on the different surfaces are also important. Fig. 6 shows the respective measurement results for the silver ink lines. The minimum line width that was possible with the used screen-printing mask was 100 µm (see Fig. 6a). The measured line width for silver ink lines with nominal widths w_n (as defined in the screen) between 100 and 400 µm is shown in Fig. 6b. It can be seen that the measured line width is always larger. The difference between the measured and nominal line widths decreases from 41 µm to 13 µm (40 % to 3 %) as the line width increases. The height profile of the silver ink shows a plateau in the middle of the line, which gets wider as the lines get wider. There are no steep edges, but flat sloping edges. From 200 µm onwards, the plateau becomes wavy. From 100–300 µm, the average line height increases from 8 µm to 16 µm as the line becomes wider.

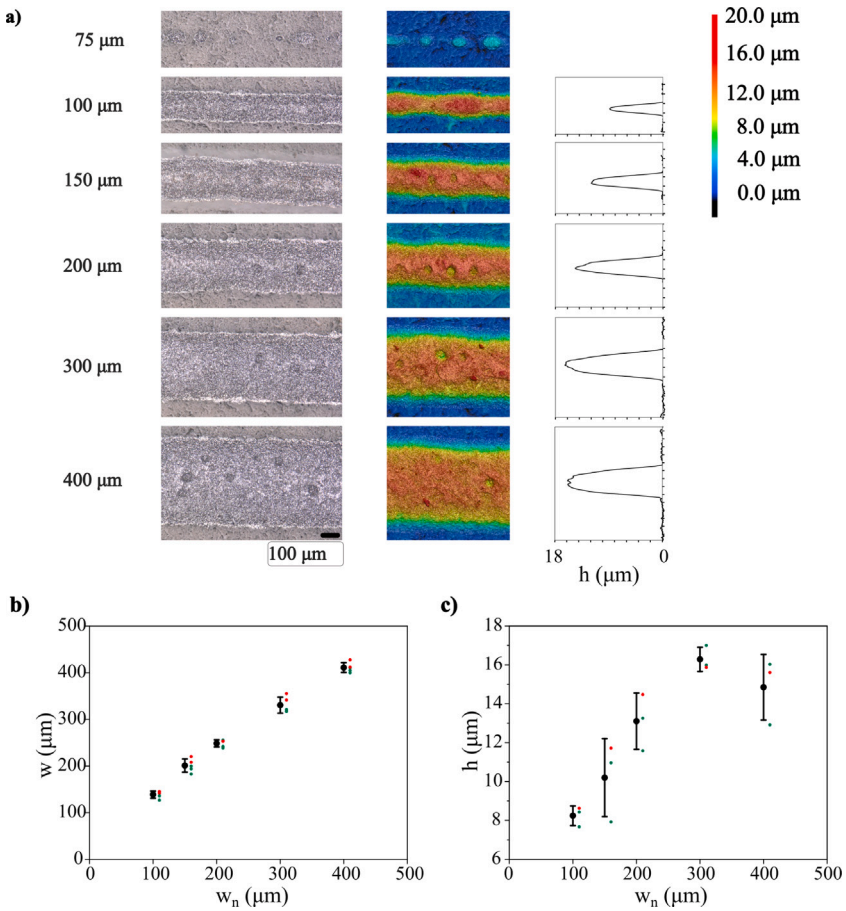

Fig. 6. Optical microscope images of silver prints with different nominal line widths on rough PEI film surface. From top to bottom: 75 µm, 100 µm, 150 µm, 200 µm, 300 µm, and 400 µm, and the corresponding height profile obtained with LSM using a profile plot with multiple lines at a distance of 1 µm across the image. (b) Measured silver line width on smooth (red, $n = 2$) and rough (green, $n = 3$) surface over nominal line width (mean ± SD, $n = 5$). (c) Measured averaged silver line height on smooth (red, $n = 1$) and rough (green, $n = 2$) surface over nominal line width (mean ± SD, $n = 3$). The colored data points have been shifted slightly to the right so that they remain visible next to the mean values.

At a line width of 500 µm, the average line height (15 µm) becomes thinner again, where the standard deviation is higher than for smaller line heights. No effect of PEI substrate roughness on the line height can be observed since the height deviation between smooth and rough surfaces is lower than the average standard deviation of line heights (7.6 % compared to 8.1 % for carbon ink lines and 5.3 % compared to 6.7 % for silver ink lines).

Fig. 7 shows the measurement results for the width w and height h of the carbon ink lines. The minimum line width that was possible with the production parameters used here was again 100 µm (see Fig. 7a). The measured line width for silver ink lines with widths between 100 and 500 µm is shown in Fig. 7c. In contrast to silver ink experiments, the measured line width was always smaller than the nominal line width w_n. For 100 µm, the actual line width was around 83 % of the nominal line width. For all other carbon line widths, the measured line width was between 93 % and 94 % of the nominal line width. The standard deviation was very low and was ≤ 1 %. The height profiles of carbon ink lines with different line widths are shown in Fig. 7a. For 100 µm and 150 µm, there is a clear maximum with steeply sloping edges. From 200 µm onwards, a plateau forms, which becomes more wavy with increasing width. For 100 µm, the line height is significantly higher (18 µm) than for 150–400 µm (16 µm, 16 µm, 16 µm, 15 µm). At 500 µm, the line height was significantly lower (11 µm). There was no significant difference in the height profile on smooth and rough substrate surfaces.

The direct contact of the mesh influences the roughness and height profile of the screen-printed ink [31]. The height profile can be explained by the mesh that is pressed onto the substrate during the screen-printing process. With higher shear viscosity and a steeper shear profile, the mesh pattern can be transferred [32]. Filaments can form when the mesh is separated after the printing process, causing locally increased thickness [33]. In this study, the mesh size was 53 µm and the wire diameter 24 µm, resulting in an opening size of 29 µm. So, with wider lines, there are more wires per line width than with narrower lines, and filaments are formed more frequently.

Our results also showed that this effect is more noticeable with the carbon ink. According to the data sheets, the used carbon ink has a higher viscosity of 18 Pa·s than the silver ink (10-15 Pa·s). In addition, as we observed in SEM images, the carbon ink also has larger particles than the silver ink. The lower viscosity of the silver ink means that it levels slightly after printing. Other groups have already shown that the viscosity of the ink influences the uniformity and roughness of the printed film on the PET substrate, as less viscous inks can still equalize once the screen has been removed [34]. This is also the reason why the measured line width of the silver ink is wider than the nominal one and for the carbon ink only slightly. If the mesh openings become smaller than the line width, complete lines can no longer be deposited. When comparing 75 µm-lines for silver and carbon, it is noticeable that the carbon ink shows more interruptions than the silver ink. Again, this can be explained by the higher viscosity of the carbon ink.

Fig. 8 shows the calculated sheet resistance R_S from measured electrical resistance for carbon and silver ink on rough and smooth PEI surfaces. In contrast to the geometric parameters line height and width, the resistance of the carbon ink with a width of 400 µm and length of 2.5 mm differs depending on whether it is screen-printed on a rough

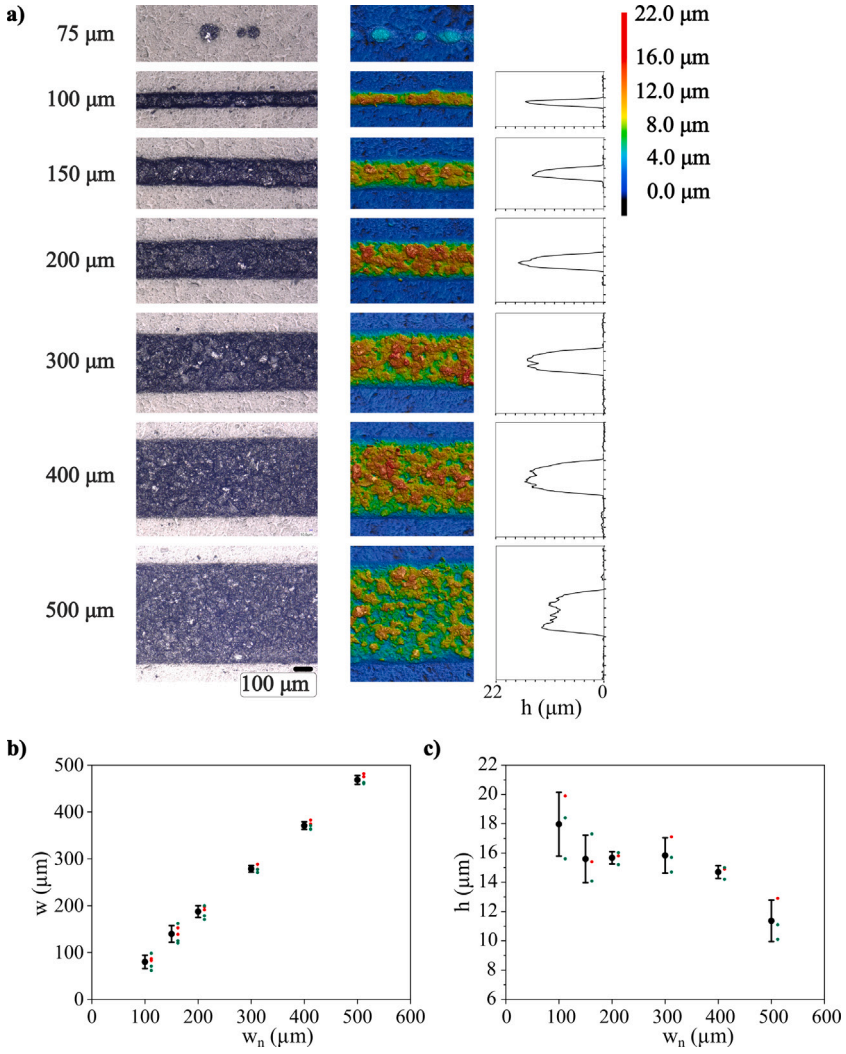

Fig. 7. (a) Optical microscope images of carbon prints with different nominal line widths on rough PEI film surface. From top to bottom: 75 µm, 100 µm, 150 µm, 200 µm, 300 µm, 400 µm and 500 µm and the corresponding height profile obtained with LSM using a profile plot with multiple lines at a distance of 1 µm across the image. (b) Measured carbon line width on smooth (red, $n = 2$) and rough (green, $n = 3$) surface over nominal line width (mean ± SD, $n = 5$). (c) Measured averaged carbon line height on smooth (red, $n = 1$) and rough (green, $n = 2$) surface over nominal line width (mean ± SD, $n = 3$). The colored data points have been shifted slightly to the right so that they remain visible next to the mean values.

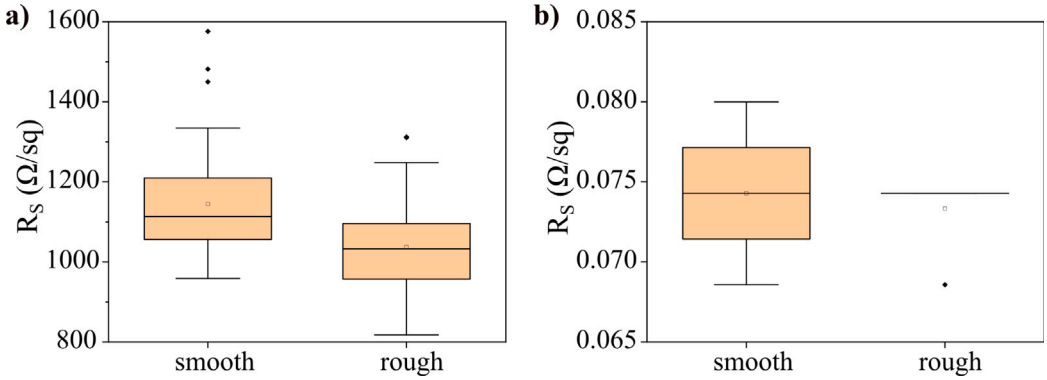

Fig. 8. Influence of surface quality on screen-printed inks: (a) calculated sheet resistance R_S of carbon ink with a nominal width of 400 µm and length of 2.5 mm ($n_{C,smooth}$=51; $n_{C,rough}$=70). (b) calculated sheet resistance R_S of silver ink with a nominal width of 400 µm and length of 7 mm ($n_{S,smooth}$=4; $n_{S,rough}$=7). The unfilled dot represents the mean. The lower and upper limits of the box are 25th and 75th percentiles and the median is between. Error bars represent the smallest and the largest value within 1.5 times the interquartile range below 25th percentile and above 75th percentile, respectively. Filled dots are outsider values.

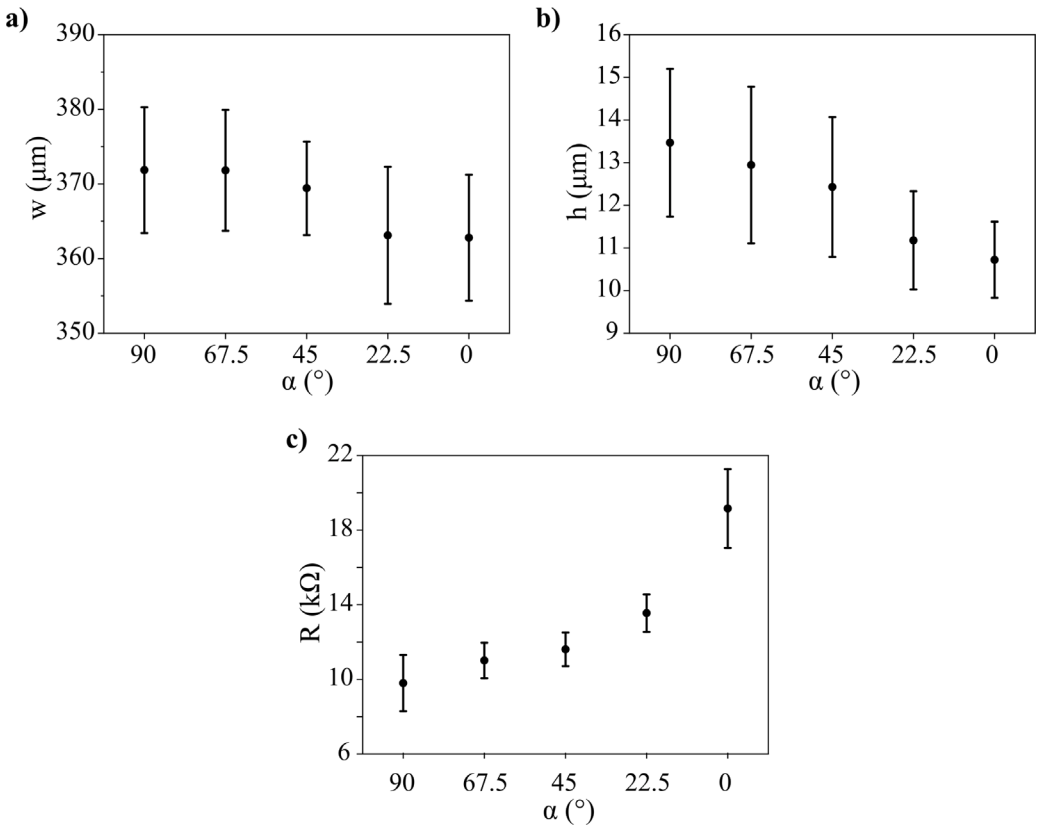

Fig. 9. Influence of the line orientation against the squeegee motion direction for carbon ink (a) measured line width (mean ± SD, $n = 5$), (b) measured line height (mean ± SD, $n = 5$), and (c) resistance (mean ± SD, $n = 5$).

or smooth surface. On the rough surface, the resistance is 10 % smaller (6.5 kΩ compared to 7.2 kΩ). The sheet resistance on smooth and rough PEI surfaces is 1.1 kΩ and 1.0 kΩ, respectively. For silver ink, there is no significant influence of the surface quality on the averaged resistance (see Fig. 8b). Here, we measured silver ink lines with 400 µm width and 7 mm length. Only the standard deviation seems to change depending on the surface quality. It becomes significantly larger with smooth surfaces (6 % compared to 3 %). On both surfaces, the resistance is significantly lower than the resistance of the carbon sensor elements, which is important if silver ink wiring is used to connect the carbon sensor elements.

Fig. 9 shows the influence of the line orientation relative to the squeegee (ink distribution tool) motion direction α on the carbon line width and height. Carbon lines with 400 µm nominal width and 7 mm length were examined. As the angle between the line and the squeegee motion direction decreases, both the line width and the line height show a trend to decrease. While these two trends do not appear significant themselves due to the large error bars, a significant trend emerges in the resistance when both geometric parameters are considered simultaneously. The average resistance increases with decreasing printing angle from 10 kΩ to 19 kΩ. This must be considered in the sensor design, particularly in the design of measuring bridges. A similar trend was not observed with silver ink. The observations can be explained by the fact that more material is stripped off at edges perpendicular to the squeegee direction unless a low viscosity leads to rapid equalization.

3.2. Characterization of sensor paths

Fig. 10a shows current–voltage (I-V) curves for the carbon sensor structures. Curves show a linear I-V-relationship, in which the slopes represent the electrical resistance R values, which are given in dependence of the nominal line width in Fig. 10b. We already know that changing the carbon conductor's line width can also change the conductor's line height. However, this effect is negligible for widths of 150–300 µm and a direct proportionality of R to $1/w$, in other words, a constant value for $R \cdot w$ can be assumed if the resistivity of the conductive material does not change. The dashed line illustrates this ideal behavior. Although the expected hyperbolic relationship appears in Fig. 10b, comparison with the reference curve reveals significant deviations for line widths of 100–300 µm, whereas the 300 and 400 µm line widths show more similar behavior. It looks more like the resistivity of the material changes with the geometry. The distribution of carbon particles in the polymer matrix is stochastic, and the formation of conductive paths can show interruptions with higher probability when conductor tracks are thin (around 15 µm according to Fig. 7c) and tracks also get very narrow. In this situation, the number of chains connecting the conductive particles without interruptions no longer scales linearly with resistor width, and conductivity will even completely break down at the percolation threshold, when the conductor cross-section becomes extremely small. This results in a far greater reduction in resistance at very small line widths than can be explained by the cross-sectional area alone.

The resistance change $\Delta R/R_0$ was recorded in dependence of longitudinal strain ε of the screen-printed carbon conductors. Here, seven conductors with different line widths w_n were measured (Fig. 11a). The data show a linear relationship between $\Delta R/R_0$ and longitudinal strain, but for thinner lines the values scatter slightly more. The slopes representing $GF = \Delta R/R_0 \cdot \varepsilon$, for the tested nominal line widths are given in Fig. 11b. The line widths have no significant influence on the sensitivity. The mean gauge factor for all line widths is around 12 with a standard deviation of less than 12 %. The material data sheet for this carbon ink provided by the vendor gives a non-linear behavior with a maximum gauge factor of 14 at a much higher strain of 100 % far beyond what was investigated here.

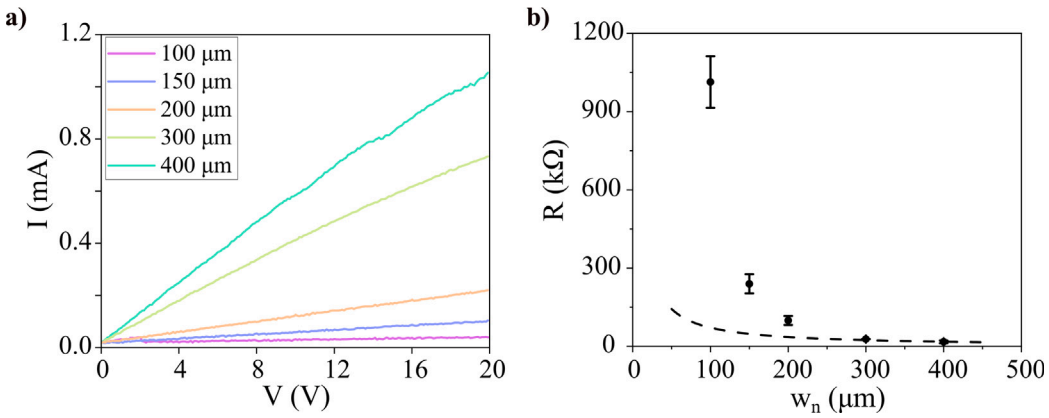

Fig. 10. Electrical characterization of carbon screen-printed conductors. (a) Current–voltage characteristic of five nominal line widths from 100 to 400 µm; (b) Electrical resistance for different nominal widths from 100 to 400 µm (mean ± SD, $n = 3$). The dashed line represents a reference curve illustrating the direct proportionality of R to $1/w$.

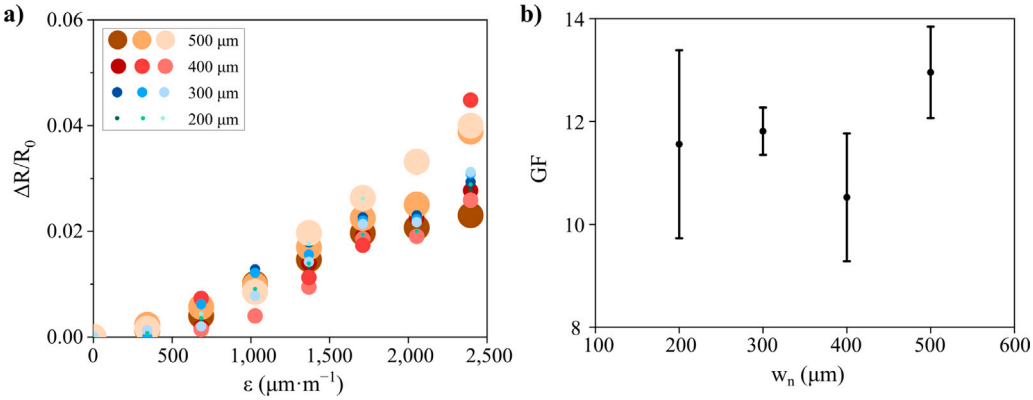

Fig. 11. Electromechanical behavior of screen-printed carbon conductors. (a) Resistance change of the screen-printed carbon conductors with line widths from 200–500 µm (three samples per line width) versus applied strain. (b) Relationship between gauge factor GF (mean ± SD, $n = 3$) for all nominal line widths in the measured strain range as function of the nominal line width.

Table 1
Young's modulus and yield strength for pure PEI samples.

Sample	Young's modulus (GPa)	Yield strength (MPa)	Elongation at yield (µm m^{-1})
1	3.5	109.1	49,200
2	3.3	109.3	51,900
3	3.3	109.0	51,600
4	3.3	109.5	51,500
5	3.4	109.1	51,300
Mean	**3.4**	**109.2**	**51,100**

Table 2
Young's modulus and yield strength for encapsulated PEI samples.

Sample	Young's modulus (GPa)	Yield strength (MPa)	Elongation at yield (µm m^{-1})
6	3.6	123.3	54,600
7	3.5	124.0	51,300
8	3.6	123.2	54,200
9	3.6	123.5	53,600
Mean	**3.6**	**123.5**	**53,425**

3.3. PEI substrate behavior

Fig. 12 shows the tensile test results (stress (σ) -strain (ε) curves) of five pure PEI specimens and four encapsulated and thus annealed PEI specimens. The strain was calculated based on crosshead displacement. The pure PEI specimens show an average yield strength of 109.2 MPa (Table 1) and the encapsulated PEI specimens of 123.5 MPa (Table 2). The Young's modulus increases from 3.4 GPa to 3.6 GPa after annealing during encapsulation.

During encapsulation, the pure PEI will be treated above the glass transition temperature 217 °C (cf. data sheet) but below the melting temperature. For thermoplastics, it is assumed that annealing above the glass transition temperature increases the crystallinity of the polymer, as the amorphous region is reconstructed. Higher crystallinity tends to result in a better tensile strength [35], as is also evident from our tests. Consequently, the pre-treatment of the PEI film at the individual production steps does not result in any reduction of the mechanical properties before the maximum load is reached. The mechanical properties after reaching the maximum load are not relevant here.

3.4. PEI smart inlay behavior

The strain-sensing performance of the PEI smart inlays (cf. Fig. 13a) was tested by straining 0.8 mm s^{-1}. According to Fig. 13b, the sensors are labeled 1L and 1R for the two sensors in the first sensor row and 2L and 2R for the two sensors in the second sensor row. An example of the sensor signal over applied strain is plotted in Fig. 13b. It can be seen that the sensor signal increases monotonically with growing applied strain. At low strains, the slope of the sensor signal is very low, as initial settlement effects occur in this range. As these settlement effects occur particularly with sensor 2R and not in the tensile tests of the pure PEI

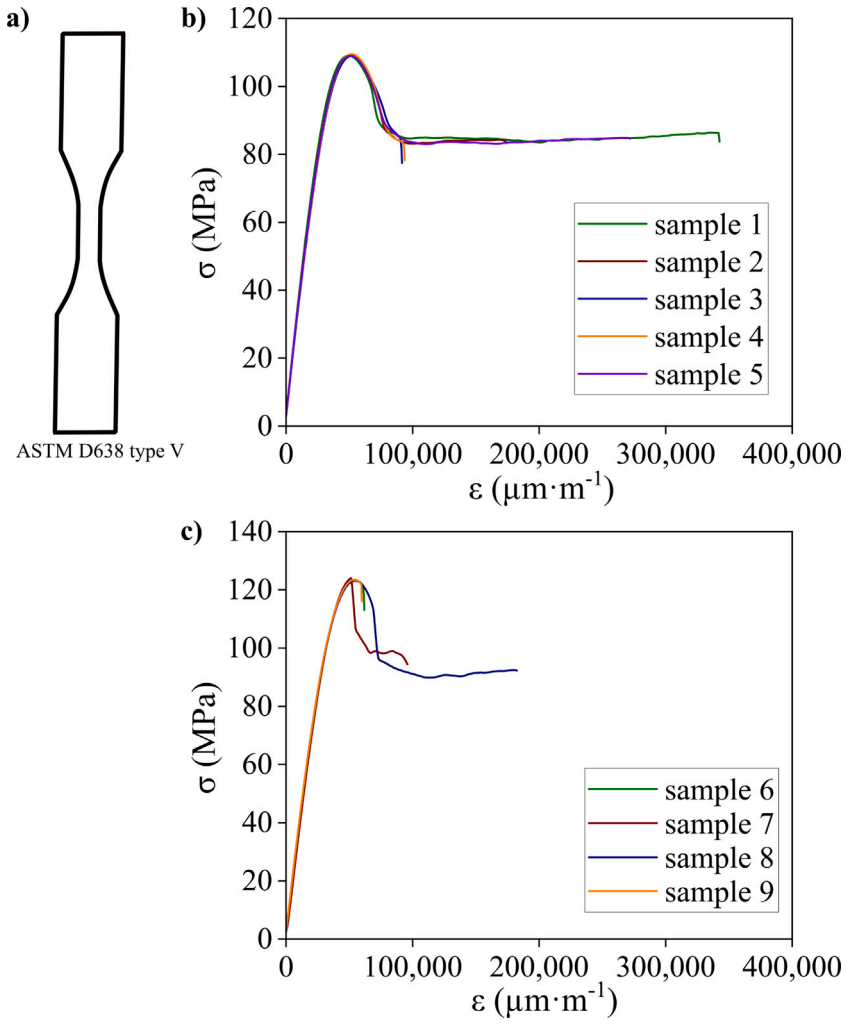

Fig. 12. Mechanical testing of PEI: (a) PEI sample (ASTM D638 type V) with a thicknesses of 125 µm for pure and of 150 µm for encapsulated PEI samples and clamping length of 25.4 mm. (b) Measured stress–strain curves of pure PEI ($n = 5$). (c) Measured stress–strain curves of encapsulated PEI ($n = 4$).

film (Fig. 12), the weight of the connector appears to have resulted in insufficient preload. With mechanical failure, the sensor signals show a sharp jump. The signals from the individual sensor bridges show that the crack runs from right to left, at around 30,000 µm·m^{-1}. Therefore, the crack started at the connector, where the weight and the sample design caused stress peaks. Fig. 13c shows the damage pattern of the PEI smart inlay after testing. To compare our results, ultimate design loads for CFRPs in the aviation industry are defined as strains between 2,500 and 4,000 µm·m^{-1} and for bonded honeycombs even as 5,000 µm·m^{-1} [20]. So, our PEI smart inlay can clearly withstand these strains, as marked in Fig. 13b. After 30,000 µm·m^{-1}, it is not the carbon sensor structures and silver conductive tracks that break, but the PEI substrate film. As written above, this is due to geometry. This can also be seen in the pure PEI film tensile tests, where elongations at break between 90,000 µm·m^{-1} and 340,000 µm·m^{-1} were achieved (Fig. 12 and Table 1). Overall, the measurements have shown that the selected screen-printing inks are functional materials with suitable mechanical properties for PEI smart inlays. Therefore, functional screen-printing inks can be used as strain sensors that can detect small to large strains.

Where a linear relationship was previously observed for smaller strains, the sensor signal shows a non-linear behavior, which can also be interpreted as more than one linear range, each with an appropriate gauge factor. Although the elongations achieved are in the range of the linear-elastic behavior of the PEI material (< 51,109 µm·m^{-1}), as shown in tensile tests of PEI films. Fig. 14a illustrates, with the representative sensor signal 2L, how the behavior of carbon strain sensors can be divided into three linear regions. In the first region with strains below 1,900 µm·m^{-1}, a gauge factor of approx. 8 is achieved (shown in Fig. 14b). In the second region with strains below 12,100 µm·m^{-1}, a gauge factor of approx. 20 is reached, and for the third region for maximum strains, the gauge factor is approx. 9. To verify reproducibility, the same measurement was carried out on three different samples. For all samples, the average gauge factor was 10 in the first linear region, 16 in the second linear region, and 9 in the third linear region. Compared to thin film sensors made of metal, these gauge factors were for all three regions much higher.

As discussed above, the carbon ink consists of an insulating polymer matrix in which carbon particles of different sizes are randomly scattered. This conductive filler forms a conductive network in the polymer matrix with a combination of contributions: the resistance of the conductive filler, the particle contact resistance, and the tunnel resistance. For the explanation of piezoresistive behavior, two theories are used. In the first, the percolation theory is based on the volume fraction of the filler. So, piezoresistivity depends on the geometrical

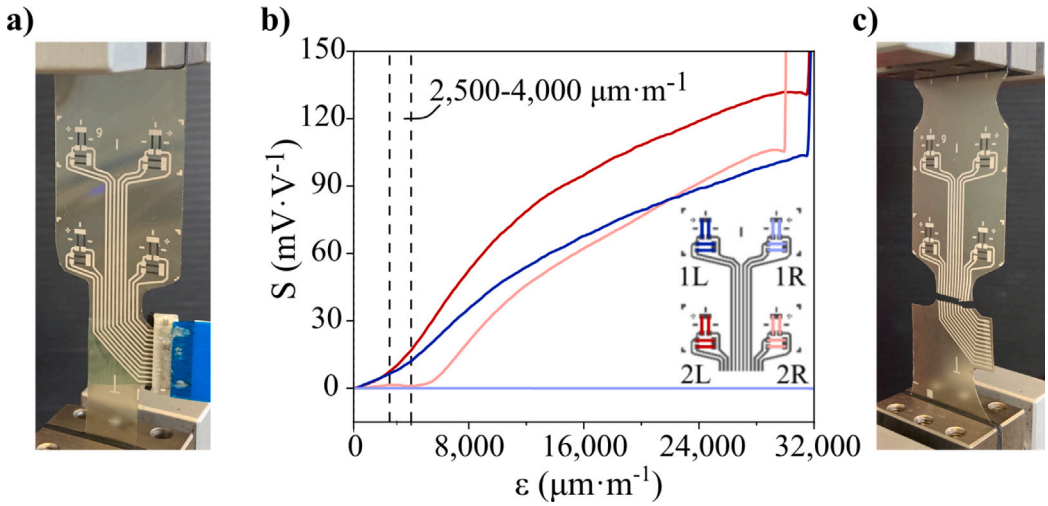

Fig. 13. Tensile testing of the smart inlay until failure: (a) PEI smart inlay clamped in the tensile testing machine. (b) Sensor signal over longitudinal strain. Sensor 1R was not working due to a connector failure. The dotted bordered area between 2,500 and 4,000 µm·m^{-1} marks defined ultimate design loads for mechanically fastened CFRPs in the aviation industry. (c) PEI smart inlay damage pattern after tensile load testing.

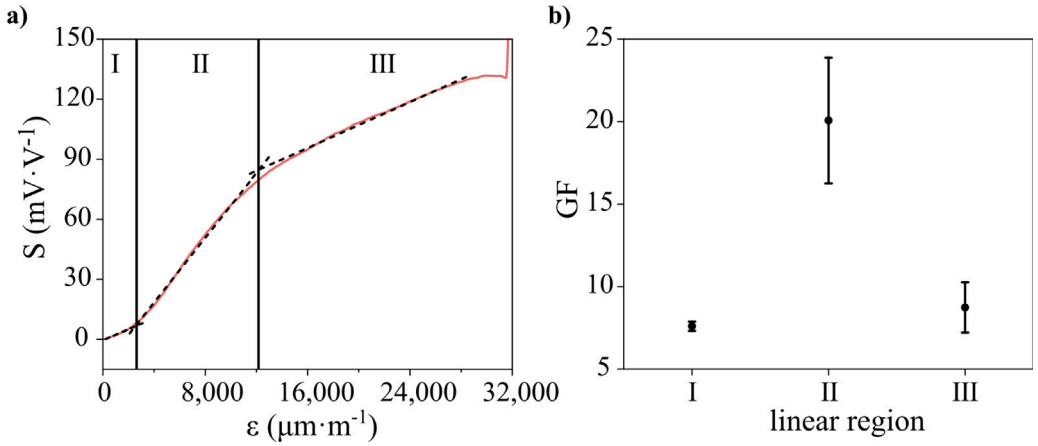

Fig. 14. (a) Sensor signal 2L versus applied strain (red line) and linear fitted curves (dashed black lines) with correlation R^2 = 0.996, R^2 = 0.995, and R^2 = 0.995 representing three linear regions. (b) Gauge factor of PEI smart inlay for the three linear regions (mean ± SD, n = 3).

properties such as filler aspect ratio and filler concentration [36]. In the second, the piezoresistive network properties are explained with the reorientation and rearrangement of particles during elongation. Recently, Ritchie et al. further investigated piezoresistivity in stretchable conductive composites with an elastomer matrix with carbon black as conductive filler [37]. They assume that the changes caused by the restructuring of the particle network are a more significant reason of piezoresistivity than only the volumetric changes.

Several studies have reported a switch in piezoresistive behavior once a critical strain is reached. The two theories mentioned above were used to explain the non-linear piezoresistive behavior of carbon-filled polymer composites by defining two, three, or even five linear regimes [38,39]. In addition, the investigation of carbon-nanotubes, carbon black in TPU matrix or polydimethylsiloxane matrix and graphene nanoplatelets in epoxy composites first showed a linear behavior at smaller strains and then an exponential/sharp increase at higher strains [8,40–42]. Others have even observed a clear decrease in resistance, i.e., a monotonically decreasing curve, when using carbon-nanotube-graphene nanoplatelet in epoxy composites above a critical strain [43]. However, according to the literature [37] restructuring of the particle network is a plausible mechanism underlying the observed piezoresistivity, as it could also explain the nonlinearity. To fully elucidate this, microstructural analysis and electromechanical characterization are needed, combined with discrete element modeling to understand the particle rearrangement and resulting changes in the current paths. For the presented carbon sensors, the division into two or three linear response regions is an empirical finding. The observed transition points are most likely associated with strain-dependent reconfiguration of the conductive network in the printed carbon ink, including changes in particle contact and tunneling distances. In addition, local microstructural damage in the sensor layer, such as the onset of microcracking, and possible changes in strain transfer within the PEI-supported inlay system may also contribute to the change in slope. However, the present experiments do not allow a direct and definite assignment of the transition points to a single physical mechanism.

3.5. Integrated PEI smart inlays

The CFRP samples with integrated smart inlays were clamped in the tensile test machine with a free length of 160 mm as presented in

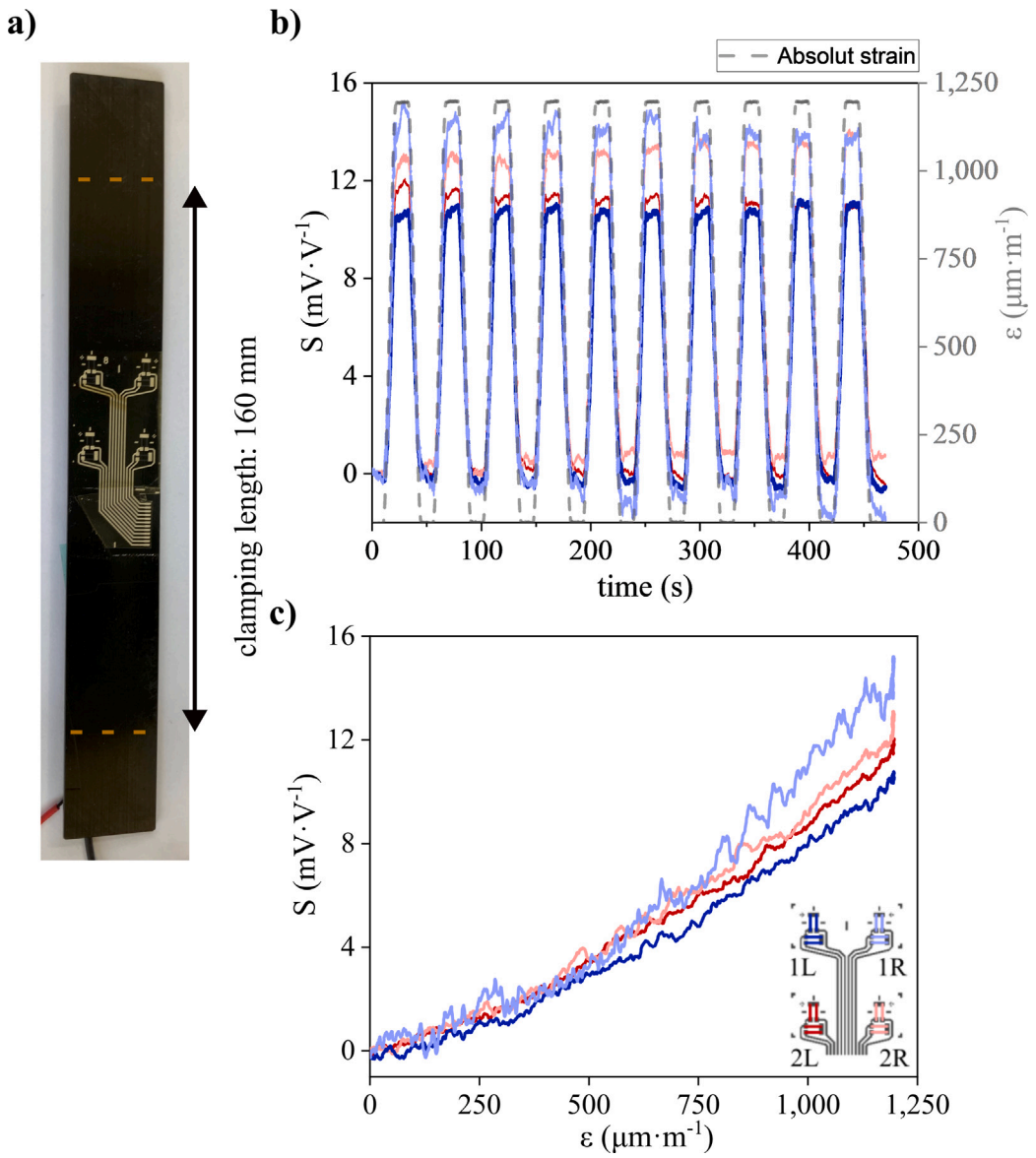

Fig. 15. Smart inlay calibration: (a) Specimen clamped into tensile testing machine with clamping length of 160 mm. (b) Sensor signal for all sensor bridges and applied strain over time. The specimen was loaded using a ramp signal up to a maximum strain of 1,196 µm·m^{-1}. (c) Representative section of the sensor signal as a function of longitudinal strain for one loading cycle.

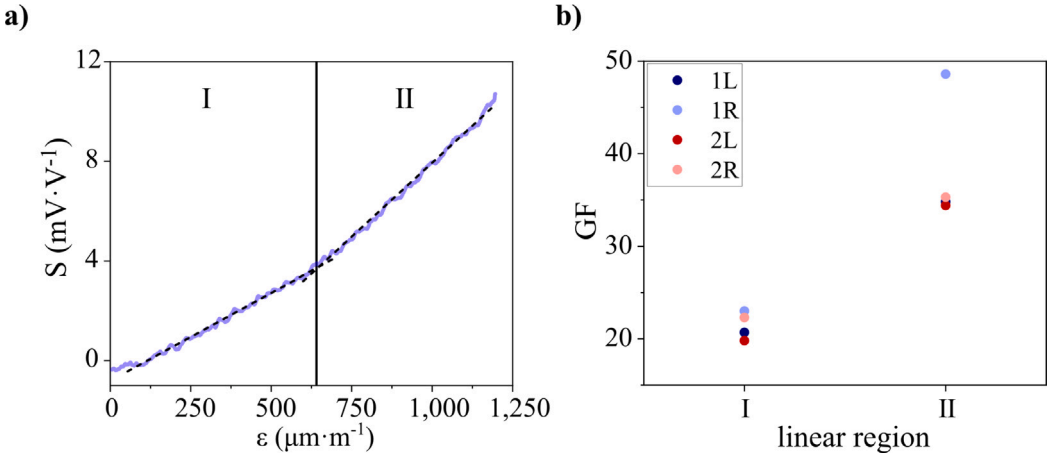

Fig. 16. (a) Mean sensor signal 1L for loading (blue line) and linear fitted curves (dashed black lines) with correlation R^2 = 0.994 and R^2 = 0.996 representing two linear regions. (b) Gauge factor versus linear region for all four sensing bridges.

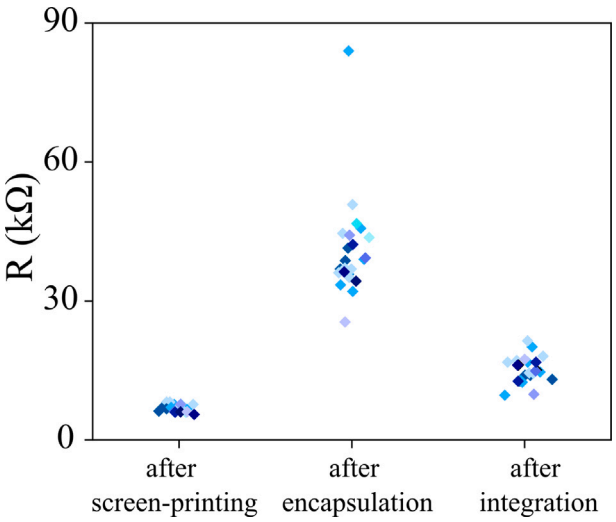

Fig. 17. Resistance of screen-printed carbon sensors (400 μm × 2.5 mm) after screen-printing and curing at 120 °C for 5 min, encapsulation at 230 °C under vacuum, and after integration at 180 °C under vacuum ($n = 24$).

Fig. 15a. As shown in longitudinal strain over time, the specimens are deflected to a maximum of 0.191 mm corresponding to a maximum longitudinal strain of 1,196 μm·m^{-1}. The longitudinal strain was again calculated based on crosshead displacement. A representative measurement and a section of this measurement of the increasing sensor signal are illustrated in Fig. 15b and 15c, respectively. The smart inlay showed a monotonic increase in the sensor signal with increasing longitudinal strain. A difference in the sensor signal between the sensor bridges on the left and right sides was observed, which is a consequence of a slight misalignment of the smart inlays within the CFRP sample. As already with the pure PEI smart inlays, a non-linear behavior was observed versus the longitudinal strain ϵ. However, compared to the observations described before, the non-linear behavior has changed. Fig. 16a shows that for the mean sensor signal 1L, the sensor signal can be divided into two linear areas. The corresponding gauge factor is shown in Fig. 16b for all four sensing bridges. For the first region, an average gauge factor of 22 was reached. For the second region, a mean gauge factor of 35 for sensing bridges 1L, 2L, and 2R was achieved. For sensing bridge 1R, the gauge factor has even reached around 49 in the second region. To verify reproducibility, the same measurement was carried out on three different samples. For all samples, the average gauge factor was 22 in the first linear region and 38 in the second linear region.

It is obvious that the sensitivity of the integrated smart inlays is significantly higher compared to the non-integrated smart inlays. We assume it is mainly related to the encapsulation, integration, and the associated annealing under harsh conditions during the autoclave process. Annealing at high temperatures leads to rearrangement of the carbon particles in the polymer matrix, resulting in an increase or decrease of resistance, depending on annealing temperature [44,45]. We also observed that the resistance initially increases by an average of 32 kΩ after encapsulation (230 °C under vacuum) and decreases by an average of 24 kΩ after integration (180 °C under vacuum), whereby the original resistance is not reached again (cf. Fig. 17). Thus, the observed resistance changes are more likely related to changes in the carbon sensor structures than to changes in the PEI film properties.

Seok Park et al. found that for carbon black in polyethylene composites, annealing below the melting temperature of the polymer matrix leads to the formation of a more crystalline phase and thus to a reduction of the amorphous regions in which the carbon black particles are dispersed, thereby reducing the distance between particles [44]. Annealing above the melting temperature, the distance between carbon black particles becomes larger [44]. Similar effects can lead to a change in resistance as observed in our case.

With the theories mentioned above, it can also be assumed that a rearrangement of the particles in the polymer matrix and thus a change in the conductive network leads to a change in the piezoresistive behavior. For multi-walled carbon nanotube in epoxy composites, it has been found in experiments that both the curing temperature and time as well as a postcuring temperature and time, influence the piezoresistivity of these composites, even at temperatures well below the annealing temperatures in this work [46]. In addition, different coefficients of thermal expansion of the used materials are also relevant. The results indicate that the annealing during encapsulation and integration appears to increase the piezoresistive response of the carbon sensors. To explain differences in the piezoresistive response between the individual tests, several factors must be taken into account. In addition to the thermomechanical history, minor printing-related deviations in sensor thickness and geometry, or local particle distribution can contribute to changes in the conductive network, including particle contact resistance and tunneling effects, as well as percolation-related transitions, and thus in piezoresistive behavior. Furthermore, contact resistance at the electrical interfaces and local strain gradients in the various test configurations can influence the measured response. The most likely cause of the observed differences in the piezoresistive behavior is therefore the thermomechanical history during encapsulation and interaction of smart inlays rather than the PEI carrier film itself or the screen-printing process.

By repeating the test ten times cyclically, the stability and repeatability of the smart inlays could also be tested. The sensor signals for loading and unloading all four sensor bridges for all ten cycles as well as the averaged sensor signals with standard deviation are illustrated in Fig. 18. The overall trend of the sensor signal of the PEI smart inlays remains the same, with only about 3.9 % ± 1.4 % repeatability error over 10 cycles and with 12.30 % ±0.99 % hysteresis.

4. Conclusion

In the present study, screen-printing ink was used to fabricate a PEI smart inlay that can be integrated in the adhesive bondline during the co-curing autoclave process. We chose highly stretchable silver and carbon composites as screen-printing inks, which we examined in detail in this work, with regard to their suitability for fabrication, design limits, and electromechanical behavior. Understanding these fabrication factors is essential for optimizing print quality and performance for sensing applications using screen-printing ink. The electromechanical and piezoresistive behavior of the sensors is non-linear, but can be linearized in separate regimes. Compared to conventional metallic strain gauges, the screen-printed stretchable carbon sensors are significantly more sensitive and achieve a maximum gauge factor of 49 on PEI integrated into CFRP. We were able to show that our smart inlays withstand the harsh conditions during co-curing in the prepreg-autoclave process and do not lose their function. The results of destructive and non-destructive static tensile tests show high elongation at break of smart inlays as the smart inlays withstand up to 30,000 μm m^{-1}. In addition, the sensor behavior is highly reproducible. With these results, we are confident that the monitoring of crack initiation and progression by our smart inlays can also be demonstrated in cycling crack growing tests, which will prove the broad applicability of this SHM approach. For future applications, the fabrication of our smart inlays is now significantly faster with fewer steps and therefore more cost-efficient, compared to our previous work using lithographic microfabrication. Screen-printing can now also be used for production scale-up and significantly larger sensor networks.

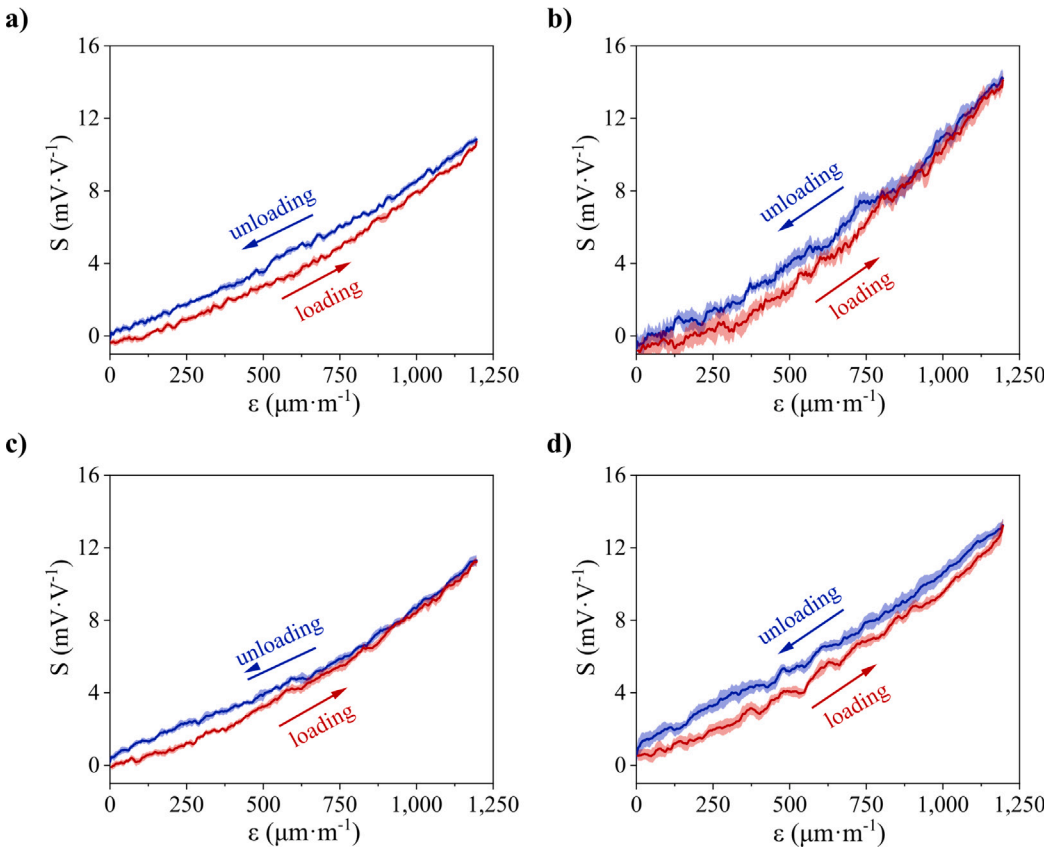

Fig. 18. Sensor signals under loading and unloading of all ten cycles and averaged sensor signal (mean ± SD, $n = 10$) for: (a) 1L. (b) 1R. (c) 2L. (d) 2R.

CRediT authorship contribution statement

Ann-Kathrin Klein: Writing – review & editing, Writing – original draft, Visualization, Validation, Methodology, Investigation, Formal analysis, Data curation. **Riem Kilian:** Writing – review & editing, Investigation. **Chresten von der Heide:** Writing – review & editing. **Julian Steinmetz:** Writing – review & editing. **Christian Hühne:** Writing – review & editing, Supervision, Project administration, Funding acquisition, Conceptualization. **Oliver Völkerink:** Writing – review & editing, Supervision, Resources, Project administration. **Andreas Dietzel:** Writing – review & editing, Supervision, Resources, Project administration, Funding acquisition, Conceptualization.

Declaration of competing interest

The authors declare the following financial interests/personal relationships which may be considered as potential competing interests: The authors declare that they have no known competing financial interests or personal relationships that could have appeared to influence the work reported in this paper.

Acknowledgments

This research was funded by the Deutsche Forschungsgemeinschaft (DFG, German Research Foundation) - 401136681.

Data availability

The raw and processed data required to reproduce the above findings are available to download from https://doi.org/10.5281/zenodo.15479526.

References

[1] C.-S. Shin, T.-C. Lin, Hygrothermal damage monitoring of composite adhesive joint using the full spectral response of fiber Bragg grating sensors, Polymers 14 (3) (2022) http://dx.doi.org/10.3390/polym14030368.
[2] W. Li, G. Palardy, Damage monitoring methods for fiber-reinforced polymer joints: A review, Compos. Struct. 299 (2022) 116043, http://dx.doi.org/10.1016/j.compstruct.2022.116043.
[3] N. Grundmann, H. Brüning, K. Tserpes, T. Strohbach, B. Mayer, Influence of embedding fiber optical sensors in CFRP film adhesive joints on bond strength, Sensors (Basel, Switzerland) 20 (6) (2020) http://dx.doi.org/10.3390/s20061665.
[4] S. Yashiro, J. Wada, Y. Sakaida, A monitoring technique for disbond area in carbon fiber–reinforced polymer bonded joints using embedded fiber Bragg grating sensors: Development and experimental validation, Struct. Health Monit. 16 (2) (2017) 185–201, http://dx.doi.org/10.1177/1475921716669979.
[5] C.S. Shin, Y.J. Yang, S.K. Liaw, Monitoring fatigue damage of an adhesive joint using fiber optics sensors, J. Phys.: Conf. Ser. 843 (2017) 012032, http://dx.doi.org/10.1088/1742-6596/843/1/012032.
[6] J. Weiland, M. Luber, K. Rostan, A. Schiebahn, R. Engelbrecht, U. Reisgen, Strain monitoring of a structural adhesive bond by embedding a polymer optical fiber, in: P. Rizzo, A. Milazzo (Eds.), European Workshop on Structural Health Monitoring, in: Lecture Notes in Civil Engineering, vol. 253, Springer International Publishing, Cham, 2023, pp. 745–754, http://dx.doi.org/10.1007/978-3-031-07254-3_75.
[7] C.-S. Shin, L.-W. Chen, Damage monitoring of composite adhesive joint integrity using conductivity and fiber Bragg grating, Polymers 15 (6) (2023) http://dx.doi.org/10.3390/polym15061575.
[8] X.F. Sánchez-Romate, C. García, J. Rams, M. Sánchez, A. Ureña, Structural health monitoring of a CFRP structural bonded repair by using a carbon nanotube modified adhesive film, Compos. Struct. 270 (2021) 114091, http://dx.doi.org/10.1016/j.compstruct.2021.114091.
[9] T. Bregar, D. An, S. Gharavian, M. Burda, I. Durazo-Cardenas, V.K. Thakur, D. Ayre, M. Słoma, M. Hardiman, C. McCarthy, H. Yazdani Nezhad, Carbon nanotube embedded adhesives for real-time monitoring of adhesion failure in high performance adhesively bonded joints, Sci. Rep. 10 (1) (2020) 16833, http://dx.doi.org/10.1038/s41598-020-74076-y.
[10] S. Qu, Y. Dai, D. Zhang, Q. Li, T.-W. Chou, W. Lyu, Carbon nanotube film based multifunctional composite materials: an overview, Funct. Compos. Struct. 2 (2) (2020) 022002, http://dx.doi.org/10.1088/2631-6331/ab9752.

[11] X. Yang, L. Sun, B. Huang, B. Zhan, C. Zhang, Y. Chu, D. An, Tuning the properties of functional adhesives with hybrid nanofillers for structural health monitoring, J. Adhes. 97 (2) (2021) 101–116, http://dx.doi.org/10.1080/00218464.2019.1638771.

[12] M. Kadlec, R. Růžek, P. Bělský, Concurrent use of Z-pins for crack arrest and structural health monitoring in adhesive-bonded composite lap joints, Compos. Sci. Technol. 188 (2020) 107967, http://dx.doi.org/10.1016/j.compscitech.2019.107967.

[13] Q. Liu, H. Sun, T. Wang, X. Qing, On-site health monitoring of composite bolted joint using built-in distributed eddy current sensor network, Mater. (Basel, Switzerland) 12 (17) (2019) http://dx.doi.org/10.3390/ma12172785.

[14] Q. Liu, H. Sun, Y. Chai, J. Zhu, T. Wang, X. Qing, On-site monitoring of bearing failure in composite bolted joints using built-in eddy current sensing film, J. Compos. Mater. 55 (14) (2021) 1893–1905, http://dx.doi.org/10.1177/0021998320979737.

[15] R.O. Ogunleye, S. Rusnáková, J. Javořík, M. Žaludek, B. Kotlánová, Advanced sensors and sensing systems for structural health monitoring in aerospace composites, Adv. Eng. Mater. 26 (22) (2024) http://dx.doi.org/10.1002/adem.202401745.

[16] B. Meemary, D. Vasiukov, M. Deléglise-Lagardère, S. Chaki, Sensors integration for structural health monitoring in composite pressure vessels: A review, Compos. Struct. 351 (2025) 118546, http://dx.doi.org/10.1016/j.compstruct.2024.118546.

[17] D. Wang, R. Yao, X. Zong, T.Y. Wong, Z. Cui, F. Zou, Y. Xiang, J. Shi, Piezoresistive intrinsic sensing methods for structural health monitoring of composites, Sensors Actuators A: Phys. 396 (2025) 117122, http://dx.doi.org/10.1016/j.sna.2025.117122.

[18] V. Kostopoulos, N. Sarantinos, S. Tsantzalis, Review of through-the-thickness reinforced z-pinned composites, J. Compos. Sci. 4 (1) (2020) 31, http://dx.doi.org/10.3390/jcs4010031.

[19] P.M. Ferreira, M.A. Machado, M.S. Carvalho, C. Vidal, Embedded sensors for structural health monitoring: Methodologies and applications review, Sensors (Basel, Switzerland) 22 (21) (2022) http://dx.doi.org/10.3390/s22218320.

[20] C. von der Heide, J. Steinmetz, M.J. Schollerer, C. Hühne, M. Sinapius, A. Dietzel, Smart inlays for simultaneous crack sensing and arrest in multifunctional bondlines of composites, Sensors 21 (11) (2021) 3852, http://dx.doi.org/10.3390/s21113852.

[21] C. von der Heide, J. Steinmetz, O. Völkerink, P. Makiela, C. Hühne, M. Sinapius, A. Dietzel, Polyetherimide-reinforced smart inlays for bondline surveillance in composites, Polymers 14 (18) (2022) http://dx.doi.org/10.3390/polym14183816.

[22] C. von der Heide, Integrable Sensors on Foil for Smart Systems and Bondline Surveillance (Ph.D. thesis), Shaker, 2024, http://dx.doi.org/10.24355/dbbs.084-202409191116-0.

[23] J. Steinmetz, Functional Compliance of Multifunctional Bondlines with Disbond Arrest and Health Monitoring Features for Safe and Efficient Composite Joints, first ed., in: Mechanics and Adaptronics, Springer International Publishing, [S.l.], 2025.

[24] D. Quan, U. Farooq, G. Zhao, C. Dransfeld, R. Alderliesten, Co-cured carbon fibre/epoxy composite joints by advanced thermoplastic films with excellent structural integrity and thermal resistance, Int. J. Adhes. Adhes. 118 (2022) 103247, http://dx.doi.org/10.1016/j.ijadhadh.2022.103247.

[25] E. Tsiangou, S. Teixeira de Freitas, I. Fernandez Villegas, R. Benedictus, Investigation on energy director-less ultrasonic welding of polyetherimide (PEI)-to epoxy-based composites, Compos. Part B: Eng. 173 (2019) 107014, http://dx.doi.org/10.1016/j.compositesb.2019.107014.

[26] A. Kyriazis, K. Asali, M. Sinapius, K. Rager, A. Dietzel, Adhesion of multifunctional substrates for integrated cure monitoring film sensors to carbon fiber reinforced polymers, J. Compos. Sci. 4 (3) (2020) 138, http://dx.doi.org/10.3390/jcs4030138.

[27] A. Kyriazis, J. Feder, K. Rager, C. von der Heide, A. Dietzel, M. Sinapius, Reducing the weakening effect in fibre-reinforced polymers caused by integrated film sensors, J. Compos. Sci. 5 (10) (2021) 256, http://dx.doi.org/10.3390/jcs5100256.

[28] A. Kyriazis, R. Kilian, M. Sinapius, K. Rager, A. Dietzel, Tensile strength and structure of the interface between a room-curing epoxy resin and thermoplastic films for the purpose of sensor integration, Polymers 13 (3) (2021) http://dx.doi.org/10.3390/polym13030330.

[29] J. Steinmetz, T. Löbel, O. Völkerink, C. Hühne, M. Sinapius, C. von der Heide, A. Dietzel, The working principles of a multifunctional bondline with disbond stopping and health monitoring features for composite structures, J. Compos. Sci. 5 (2) (2021) 51, http://dx.doi.org/10.3390/jcs5020051.

[30] E. Krause, G.M. Yang, G.M. Sessler, Charge dynamics and morphology of Ultem 1000 and Ultem 5000 PEI grade films, Polym. Int. 46 (1) (1998) 59–64, http://dx.doi.org/10.1002/(SICI)1097-0126(199805)46:1{%}3C59::AID-PI986{%}3E3.0.CO;2-2.

[31] B.N. Altay, J. Jourdan, V.S. Turkani, H. Dietsch, D. Maddipatla, A. Pekarovicova, P.D. Fleming, M. Atashbar, Impact of substrate and process on the electrical performance of screen-printed nickel electrodes: Fundamental mechanism of ink film roughness, ACS Appl. Energy Mater. 1 (12) (2018) 7164–7173, http://dx.doi.org/10.1021/acsaem.8b01618.

[32] C. Phillips, A. Al-Ahmadi, S.-J. Potts, T. Claypole, D. Deganello, The effect of graphite and carbon black ratios on conductive ink performance, J. Mater. Sci. 52 (16) (2017) 9520–9530, http://dx.doi.org/10.1007/s10853-017-1114-6.

[33] S.-J. Potts, C. Phillips, T. Claypole, E. Jewell, The effect of carbon ink rheology on ink separation mechanisms in screen-printing, Coatings 10 (10) (2020) 1008, http://dx.doi.org/10.3390/coatings10101008.

[34] A. Claypole, J. Claypole, L. Kilduff, D. Gethin, T. Claypole, Stretchable carbon and silver inks for wearable applications, Nanomater. (Basel, Switzerland) 11 (5) (2021) http://dx.doi.org/10.3390/nano11051200.

[35] M. Yilmaz, N.F. Yilmaz, M.F. Kalkan, Rheology, crystallinity, and mechanical investigation of interlayer adhesion strength by thermal annealing of polyetherimide (PEI/ULTEM 1010) parts produced by 3D printing, J. Mater. Eng. Perform. 31 (12) (2022) 9900–9909, http://dx.doi.org/10.1007/s11665-022-07049-z.

[36] A.B. Oskouyi, U. Sundararaj, P. Mertiny, Tunneling conductivity and piezoresistivity of composites containing randomly dispersed conductive nano-platelets, Mater. (Basel, Switzerland) 7 (4) (2014) 2501–2521, http://dx.doi.org/10.3390/ma7042501.

[37] L. Ritchie, E. Pahl, I.A. Anderson, The incompressibility assumption and piezoresistivity in stretchable conductive composites, J. Appl. Polym. Sci. 141 (34) (2024) http://dx.doi.org/10.1002/app.55855.

[38] A. Del Bosque, X.F. Sánchez-Romate, M. Sánchez, A. Ureña, Toward flexible piezoresistive strain sensors based on polymer nanocomposites: a review on fundamentals, performance, and applications, Nanotechnology 35 (29) (2024) http://dx.doi.org/10.1088/1361-6528/ad3e87.

[39] A. Georgopoulou, F. Clemens, Piezoresistive elastomer-based composite strain sensors and their applications, ACS Appl. Electron. Mater. 2 (7) (2020) 1826–1842, http://dx.doi.org/10.1021/acsaelm.0c00278.

[40] Y. Zheng, Y. Li, K. Dai, M. Liu, K. Zhou, G. Zheng, C. Liu, C. Shen, Conductive thermoplastic polyurethane composites with tunable piezoresistivity by modulating the filler dimensionality for flexible strain sensors, Compos. Part A: Appl. Sci. Manuf. 101 (2017) 41–49, http://dx.doi.org/10.1016/j.compositesa.2017.06.003.

[41] Y. Zheng, Y. Li, Z. Li, Y. Wang, K. Dai, G. Zheng, C. Liu, C. Shen, The effect of filler dimensionality on the electromechanical performance of polydimethylsiloxane based conductive nanocomposites for flexible strain sensors, Compos. Sci. Technol. 139 (2017) 64–73, http://dx.doi.org/10.1016/j.compscitech.2016.12.014.

[42] M. Park, H. Kim, J.P. Youngblood, Strain-dependent electrical resistance of multi-walled carbon nanotube/polymer composite films, Nanotechnology 19 (5) (2008) 055705, http://dx.doi.org/10.1088/0957-4484/19/05/055705.

[43] W. Li, A. Dichiara, J. Bai, Carbon nanotube–graphene nanoplatelet hybrids as high-performance multifunctional reinforcements in epoxy composites, Compos. Sci. Technol. 74 (2013) 221–227, http://dx.doi.org/10.1016/j.compscitech.2012.11.015.

[44] J. Seok Park, P. Hyun Kang, Y. Chang Nho, D. Hack Suh, Effects of thermal ageing treatment and antioxidants on the positive temperature coefficient characteristics of carbon black/polyethylene conductive composites, J. Appl. Polym. Sci. 89 (9) (2003) 2316–2322, http://dx.doi.org/10.1002/app.11953.

[45] Y. Song, Q. Zheng, Influence of annealing on conduction of high–density polyethylene/carbon black composite, J. Appl. Polym. Sci. 105 (2) (2007) 710–717, http://dx.doi.org/10.1002/app.26076.

[46] T.Y. Wong, T. Yu, F. Zou, Effect of curing condition on the piezoresistivity of multi-walled carbon nanotube/epoxy nanocomposites, Compos. Commun. 39 (2023) 101557, http://dx.doi.org/10.1016/j.coco.2023.101557.